A dispersive coupled channels analysis of nucleon scattering from ^{181}Ta and ^{182,184,186}W up to 200 MeV

P. Romain and J.P. Delaroche

Service de Physique Nucléaire
Centre d'Études de Bruyères-le-Châtel
BP 12, 91680 Bruyères-le-Châtel, France

Abstract

The dispersive optical model approach to nucleon scattering is extended from spherical nuclei to permanently deformed nuclei for the first time. Here, a dispersive coupled channels analysis of proton and neutron scattering and reaction cross sections is presented for ^{181}Ta and ^{182,184,186}W for incident energies up to 200 MeV. A very good overall agreement between experimental data and predictions is achieved up to 65 MeV. Above this energy it is necessary to introduce an explicit treatment of the non-locality of the imaginary potential to achieve an excellent agreement.

1 Introduction

Dispersion relations (DRs) have so far been used to build mean fields of protons and neutrons in spherical nuclei. These dispersive optical model potentials (OMPs) have been quite successful in describing the nucleon single-particle properties in the bound state region and continuum over a broad energy range [1].

The dispersive OMP studies are here extended to deformed nuclei. This study is limited to positive energies, mainly for two reasons. First, single-particle strengths in deformed nuclei are considerably fragmented. Second, the spherical shell model is not appropriate for predicting bound state properties of these nuclei.

The interaction of nucleons with ^{181}Ta and ^{182,184,186}W, four nuclei at the edge of the rare-earth region, is analyzed in the coupled channels (CC) framework for incident energies up to 200 MeV. This analysis, which requires a generalization of the usual dispersion relations, is now presented.

2 Dispersion Relations

2.1 Spherical nuclei

The complex mean field of a nucleon in a spherical nucleus is usually defined as

$$\begin{aligned}\mathcal{U}(r,r',E) &= \mathcal{V}_{HF}(r,r') + \frac{P}{\pi}\int \frac{\mathcal{W}(r,r',E')}{E'-E}dE' + i\mathcal{W}(r,r',E) \\ &= \mathcal{V}_{HF}(r,r') + \Delta\mathcal{V}_{\mathcal{W}}(r,r',E) + i\mathcal{W}(r,r',E), \end{aligned} \quad (1)$$

where $\mathcal{V}_{HF}(r,r')$ is a smooth potential (this term corresponds to the so-called Hartree-Fock (HF) potential in phenomenological OMP analyses), $\Delta\mathcal{V}_{\mathcal{W}}(r,r',E)$ the dispersive term, and $\mathcal{W}(r,r',E)$ the absorptive potential. Here P stands for principal value. $\mathcal{U}(r,r',E)$ is non-local and energy dependent. Through a Wigner transformation, $\mathcal{U}$ may be expressed in terms of the momentum k

$$\tilde{\mathcal{U}}(r,k,E) = \tilde{\mathcal{V}}_{HF}(r,k) + \Delta\tilde{\mathcal{V}}_{\mathcal{W}}(r,k,E) + i\tilde{\mathcal{W}}(r,k,E). \quad (2)$$

The OMP is closely related to $\tilde{\mathcal{U}}(r,k(r,E),E)$ which stems from the on-shell approximation:

$$k^2(r,E) \approx (\frac{2\mu}{\hbar^2})[E - \tilde{\mathcal{V}}_{HF}(r,k(r,E))], \tag{3}$$

where $\tilde{\mathcal{V}}_{HF}(r,k(r,E)) \equiv V_{HF}(r,E)$ is the local-equivalent HF potential and μ the reduced mass.

In the calculation of DR terms, only the explicit dependence on E of the imaginary potential should be considered. This means that the dependences upon k and E should be disentangled before the on-shell approximation is performed. Assuming a Perey and Buck type of non-locality [2] for the absorption, it follows that the DR terms to be used in phenomenological OMP analyses are written as [3]

$$\Delta V_i(r,E) = e^{-\beta^2 k^2(r,E)/4} \frac{P}{\pi} \int \frac{e^{+\beta^2 k^2(r,E')/4} W_i(r,E')}{E' - E} dE', \tag{4}$$

where β is the non-locality range, and where W_i stands for the surface ($i = D$) or volume ($i = V$) absorption. In our analysis, eq.(4) has been used only for the surface absorption. Including the non-locality of W_V into the calculation of ΔV_V would result in a renormalization of the Hartree-Fock term. Therefore, ΔV_V is calculated assuming $\beta = 0$ in eq.(4).

The on-shell momentum $k(r,E))$ defined in eq.(3) and entering into eq.(4) depends upon the "Hartree-Fock" potential. For $V_{HF}(r,E)$, we adopt a form inspired from the Perey and Buck approximation

$$V_{HF}(r,E) = V_0 e^{-\beta_0^2 \frac{\mu}{2\hbar^2}[E - V_{HF}(r=0,E)] + \beta_1^2 \frac{4\mu^2}{\hbar^4}[E - V_{HF}(r=0,E)]^2} f(r), \tag{5}$$

where $f(r)$ is a Woods-Saxon shape, and β_0 and β_1 two parameters which mimic an E-dependent range of non-locality for V_{HF}.

2.2 Deformed nuclei

In the body-fixed system of coordinates of the nucleus, the complex mean field felt by a nucleon is

$$\begin{aligned} \mathcal{U}(\overrightarrow{r}, \overrightarrow{r}', E) &= \mathcal{V}_{HF}(\overrightarrow{r}, \overrightarrow{r}') + \frac{P}{\pi} \int \frac{\mathcal{W}(\overrightarrow{r}, \overrightarrow{r}', E')}{E' - E} dE' + i\mathcal{W}(\overrightarrow{r}, \overrightarrow{r}', E) \\ &= \mathcal{V}_{HF}(\overrightarrow{r}, \overrightarrow{r}') + \Delta\mathcal{V}_{\mathcal{W}}(\overrightarrow{r}, \overrightarrow{r}', E) + i\mathcal{W}(\overrightarrow{r}, \overrightarrow{r}', E). \end{aligned} \tag{6}$$

Treating the radial coordinates and momentum as independent variables, a Wigner transform leads to

$$\tilde{\mathcal{U}}(\overrightarrow{r}, \overrightarrow{k}, E) = \tilde{\mathcal{V}}_{HF}(\overrightarrow{r}, \overrightarrow{k}) + \Delta\tilde{\mathcal{V}}_{\mathcal{W}}(\overrightarrow{r}, \overrightarrow{k}, E) + i\tilde{\mathcal{W}}(\overrightarrow{r}, \overrightarrow{k}, E). \tag{7}$$

The deformed OMP is again closely related to $\tilde{\mathcal{U}}(\overrightarrow{r}, \overrightarrow{k}(\overrightarrow{r}, E), E)$ through the on-shell approximation

$$k^2(\overrightarrow{r}, E) \approx (\frac{2\mu}{\hbar^2})[E - \tilde{\mathcal{V}}_{HF}(\overrightarrow{r}, k(\overrightarrow{r}, E))], \tag{8}$$

where $\tilde{\mathcal{V}}_{HF}(\overrightarrow{r}, k(\overrightarrow{r}, E)) \equiv V_{HF}(\overrightarrow{r}, E)$ is the local-equivalent, deformed HF potential.

Following the same reasoning as before for spherical nuclei, the dispersive (surface) term writes

$$\Delta V_D(\overrightarrow{r}, E) = e^{-(\frac{\beta^2\mu}{2\hbar^2})[E - V_{HF}(\overrightarrow{r}, E)]} \frac{P}{\pi} \int \frac{e^{+(\frac{\beta^2\mu}{2\hbar^2})[E' - V_{HF}(\overrightarrow{r}, E')]} W_D(\overrightarrow{r}, E')}{E' - E} dE', \tag{9}$$

in which the deformed HF potential is parameterized as

$$V_{HF}(\overrightarrow{r}, E) = V_{HF}(E) f(r, a_V, R_V). \tag{10}$$

In eq.(10), $f(r, a_V, R_V)$ is a deformed Woods-Saxon shape

$$f(r, a_V, R_V) \frac{1}{1 + e^{\frac{r - R_V}{a_V}}}, \tag{11}$$

with

$$R_V = r_V A^{\frac{1}{3}}[1 + \beta_2^V Y_{20}(\Omega') + \beta_4^V Y_{40}(\Omega')], \tag{12}$$

where β_2^V and β_4^V are quadrupole and hexadecapole deformations, respectively, and where the angle Ω' refers to the body-fixed system.

The coupled channels calculations require that the deformed OMP be expanded into spherical harmonics. For $\Delta V_D(\overrightarrow{r}, E)$, this expansion reads

$$\Delta V_D(\overrightarrow{r}, E) = \sum_{\Lambda \geq 0} \Delta V_D^{\Lambda}(r, E) Y_{\Lambda 0}(\Omega'), \tag{13}$$

where

$$\Delta V_D^{\Lambda}(r, E) = e^{-(\frac{\beta^2 \mu}{2\hbar^2})E} \sum_{l,l',j,\lambda} \frac{(2j+1)\hat{l}\hat{l}'\hat{\lambda}\hat{\Lambda}}{4\pi^2} \begin{pmatrix} l & l' & j \\ 0 & 0 & 0 \end{pmatrix}^2 \begin{pmatrix} j & \lambda & \Lambda \\ 0 & 0 & 0 \end{pmatrix}^2$$

$$\times A^{\lambda}(r, E) P \int \frac{e^{+(\frac{\beta^2 \mu}{2\hbar^2})E'} B^{l'}(r, E') W_D^{l}(r, E')}{E' - E} dE', \tag{14}$$

in which $A^{\lambda}(r, E)$, $B^{l'}(r, E')$ and $W_D^{l}(r, E')$ are coefficients of the expansions of $e^{+(\frac{\beta^2 \mu}{2\hbar^2})[V_{HF}(\overrightarrow{r}, E)]}$, $e^{-(\frac{\beta^2 \mu}{2\hbar^2})[V_{HF}(\overrightarrow{r}, E')]}$ and $W_D(\overrightarrow{r}, E')$, respectively, and $\hat{l} = \sqrt{2l+1}$.

The CC calculations are performed using Raynal's `ECIS95` code run in the external input mode [4]. All the calculations are performed using DR terms calculated in the subtracted form

$$\Delta V_D(\overrightarrow{r}, E) = \frac{P}{\pi} \int_{-\infty}^{+\infty} W_D(\overrightarrow{r}, E') (\frac{1}{E' - E} - \frac{1}{E' - E_F}) dE', \tag{15}$$

where E_F is the Fermi energy.

3 Dispersive deformed optical potential

In our analysis, the geometry parameters of all potentials remained fixed for all energies and were assumed identical for the real and imaginary volume terms. The deformed optical potential for neutrons and protons is written as

$$U(\overrightarrow{r}, E) = -(V_{HF}(E) + \Delta V_V(E) + iW_V(E)) f(r, a_V, R_V)$$

$$+4a_D(\Delta V_D(E) + iW_D(E)) \frac{d}{dr} f(r, a_D, R_D) + V_C(\overrightarrow{r}, a_C, R_C)$$

$$-2i\lambda\!\!\!^{-2}_{\pi}(V_{SO}(E) + iW_{SO}(E)) \overrightarrow{\bigtriangledown} f(r, a_{SO}, R_{SO}) \times \overrightarrow{\bigtriangledown}.\overrightarrow{s}, \tag{16}$$

where the strengths of the real potential, the volume and surface absorptions, and the real and imaginary spin-orbit potentials are $\{V_{HF}, \Delta V_V, \Delta V_D\}, W_V, W_D, V_{SO}, W_{SO}$, respectively. V_C is the Coulomb potential ($V_C = 0$ for neutrons).

The radial form factors $f(r, a_i, R_i)$ $(i = V, D, SO, C)$ are Woods-Saxon types (see eq.11), and the deformation lengths δ_λ $(\lambda = 2, 4)$ are kept identical for all the potential terms

$$\delta_\lambda = \beta_\lambda^V r_V A^{\frac{1}{3}} = \beta_\lambda^W r_W A^{\frac{1}{3}} = \beta_\lambda^D r_D A^{\frac{1}{3}} = \beta_\lambda^{SO} r_{SO} A^{\frac{1}{3}} = \beta_\lambda^C r_C A^{\frac{1}{3}}. \tag{17}$$

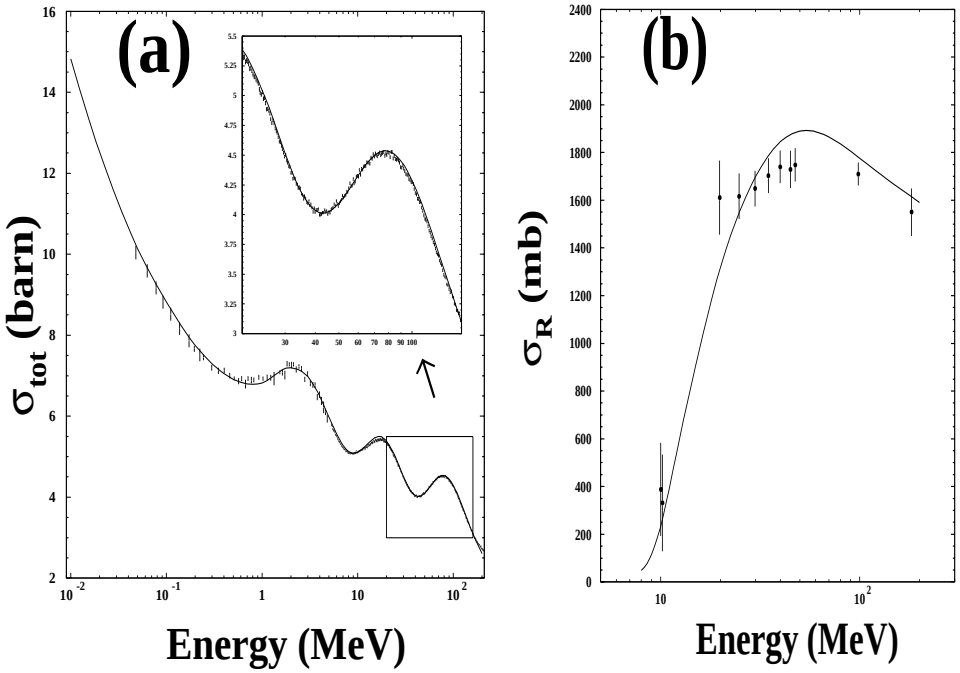

Figure 1: (a) Neutron total cross section and (b) proton reaction cross section for ^{181}Ta. Comparisons between experimental data and present calculations, which include a treatment of the non-locality of the surface absorption.

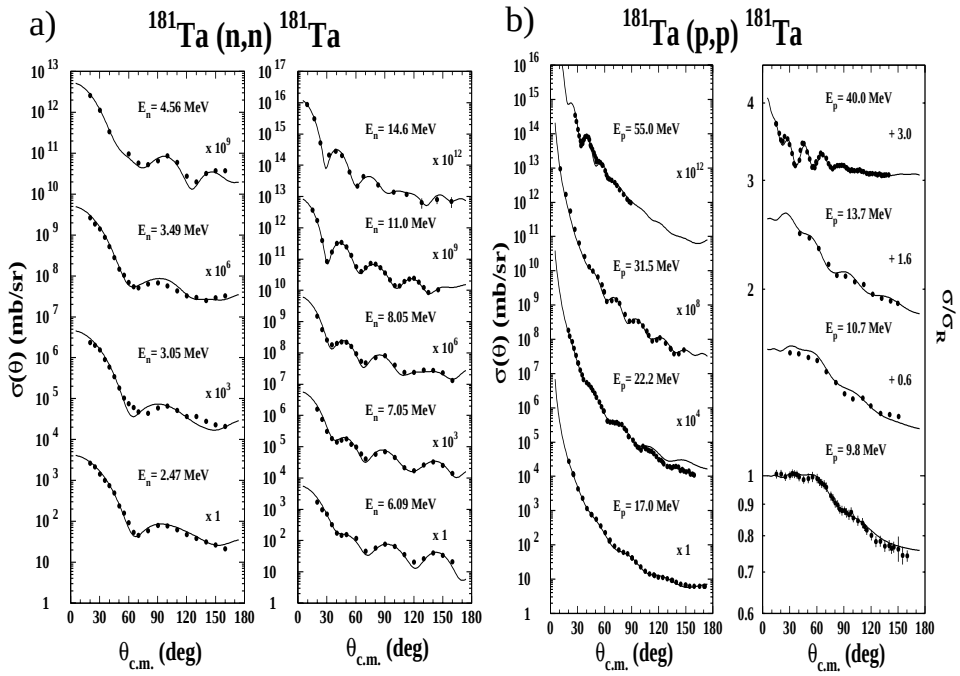

Figure 2: Comparisons between measured elastic differential scattering cross sections and present CC calculations including a treatment of the non-locality of the surface absorption for (a) n + ^{181}Ta and (b) p + ^{181}Ta systems.

4 Data analyses

4.1 Neutron + ^{181}Ta

The data set which we used in the CC analyses consists of neutron elastic scattering differential cross sections between 2.47 and 14.6 MeV, and neutron total cross section for neutron energies between 50 keV and 200 MeV. We have also used the S- and P-wave strength functions S_0 and S_1 and potential scattering radius R'. Compound-nucleus contributions to the differential cross sections were calculated up to 8 MeV using the Hauser-Feshbach theory complemented with the width fluctuation factor of Moldauer.

The present analysis consisted of adjusting all potential depths and geometries. The deformation parameters have also been optimized, taking as first guesses the deformations β_2 and β_4 of ^{182}W as given in [6]. The coupling scheme includes the $7/2^+$ to $15/2^+$ states of the ground state band.

In a first step we have ignored the non-locality of W_D when calculating the DR terms. In a second step the non-locality has been included, and its range adjusted to optimize the fit to the σ_T data (see Fig.1(a)). The optimum value found for this range is $\beta = 1.2$ fm. The effect of non-locality of W_D on CC predictions increases with increasing energy. It is weak at low energy ($E \leq 20$ MeV). Including the non-locality is essential to produce an excellent fit to σ_T [5] at high energy ($E \geq 20$ MeV). When β is varied from 1.2 fm to zero, the chi-square per datum (χ^2/N) drops by a factor of 3.4 in the 20 - 160 MeV energy range. χ^2/N is slightly getting worse beyond 160 MeV. This probably means that our parameterization of $W_V(E)$ is not realistic enough above pion production threshold (see Fig.6). We also obtain a very good agreement between measured and calculated differential cross sections (see Fig.2(a)).

4.2 Proton + ^{181}Ta and proton + ^{182,184}W

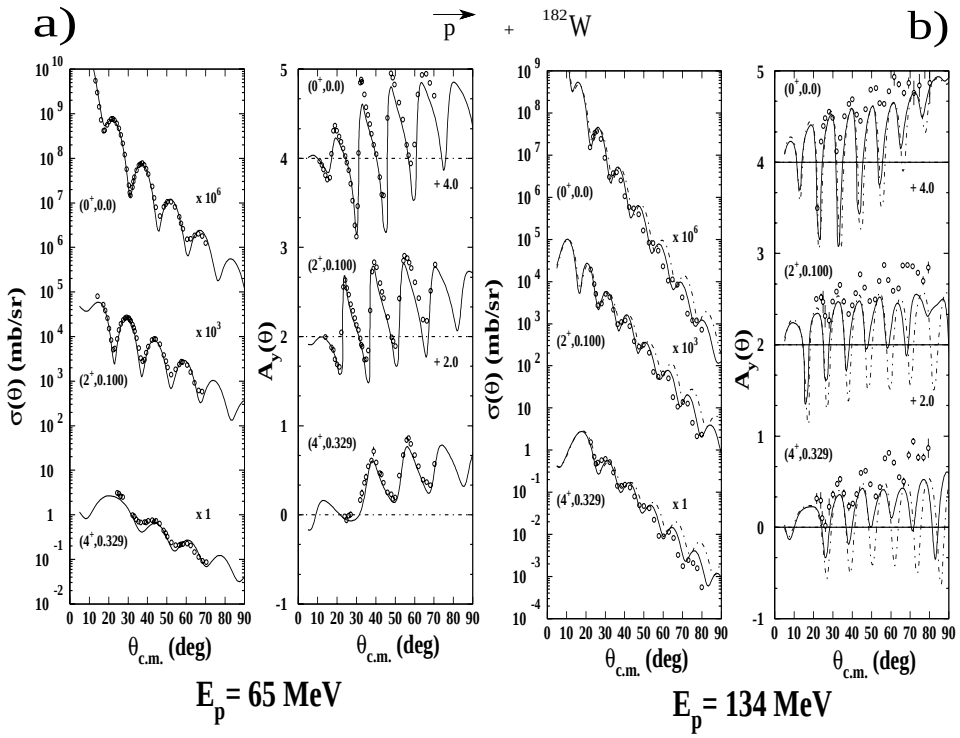

Figure 3: Proton elastic and inelastic scattering from ^{182}W at (a) E=65 MeV and (b) E=134 MeV. Comparison between measurements (dots) and CC calculations in which the range of non-locality is included (continuous curves). The dashed curves shown at E=134 MeV are obtained by setting $\beta = 0$ in the CC calculations.

The dispersive coupled channels analysis was also applied to the p+^{181}Ta and p + ^{182,184}W systems. Comparisons between the CC calculations and measured differential cross sections are presented in Figs.2(b),3(a) and 3(b). Here also our predictions compare very well with the experimental data provided the non-locality of W_D is included. The optimum value of the non-locality range is $\beta = 1.4$ fm. Without having $\beta \neq 0$, the CC predictions for ^{182}W(p,p')^{182}W* at $E = 134$ MeV badly miss the magnitude and shape of the measured [7] differential cross sections (see Fig.3(b)). On the other hand, the σ_R data for ^{181}Ta are too scarce for providing useful and complementary information on β (see Fig.1(b)).

4.3 Predictions for n + ^{182,184,186}W

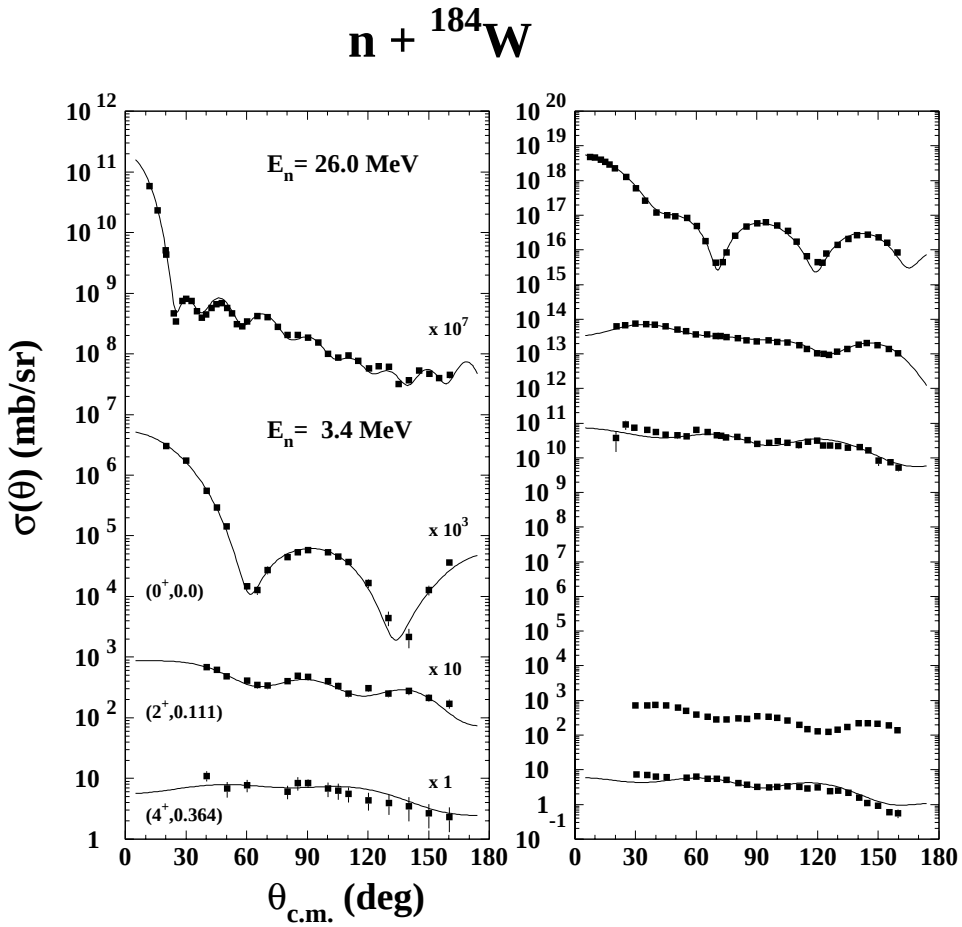

Figure 4: Neutron elastic and inelastic scattering from ^{184}W at 3.4, 4.87, 6.0 and 26 MeV. Comparison between experimental data and present predictions.

The above deformed neutron OMP tailored to fit the n + ^{181}Ta experimental data is now used to predict scattering and reaction cross sections for neutrons incident on the isotopes ^{182,184,186}W and elemental tungsten ^{nat}W.

Because the asymmetry parameter $\alpha = \frac{N-Z}{A}$ for ^{181}Ta ($\alpha_{181} = 0.193$) is nearly identical to that for ^{184}W ($\alpha_{184} = 0.196$) the following relation holds for the OMPs

$$U(n +^{181} Ta) \approx U(n +^{184} W).$$

For simplicity, we assume the same property to be valid for the other W isotopes. Only the deformation

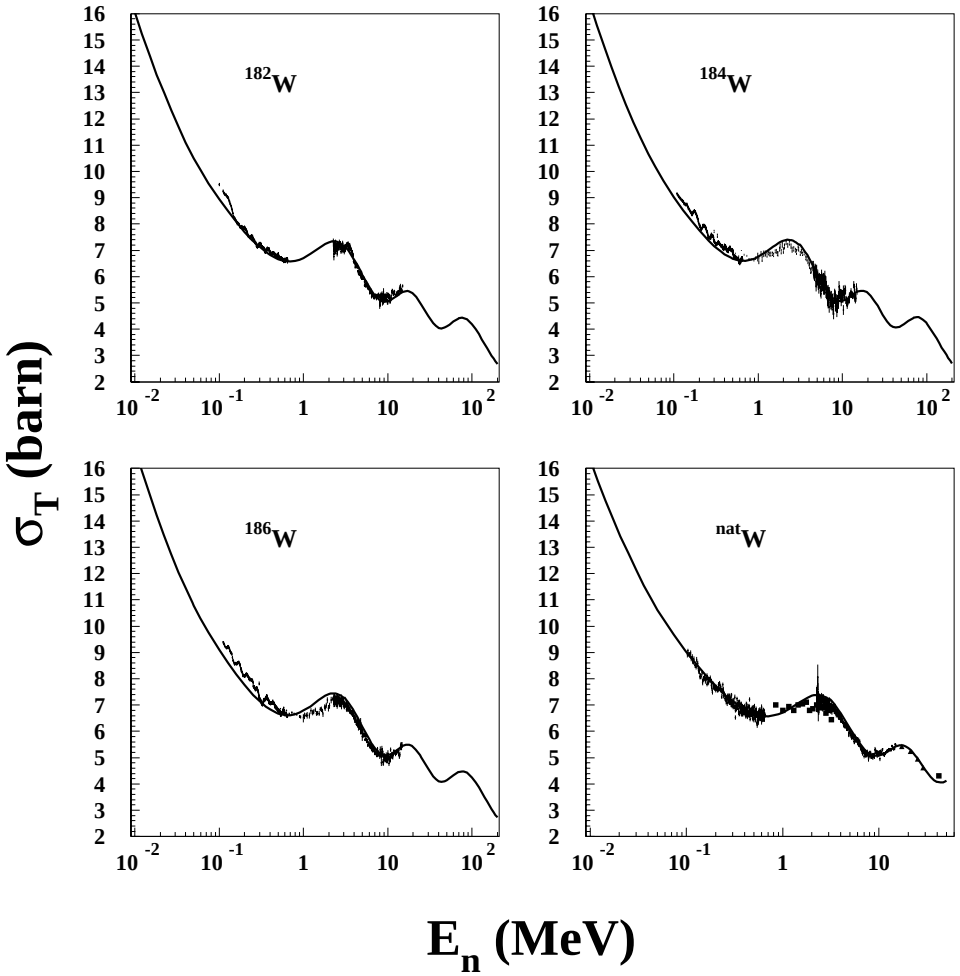

Figure 5: Neutron total cross sections for W isotopes. Comparisons between experimental data and present CC predictions, which include a treatment of the non-locality of the surface absorption.

parameters β_2 and β_4 of each isotope will differ in the CC calculations. The parameters used in the present calculations have values close to those published earlier [6].

In Fig.4 are shown our predictions for ^{184}W and comparisons with measured elastic and inelastic scattering cross sections. As can be seen, the predictions compare very well with the data. This comparison is extended to total cross sections in Fig.5. Again, the agreement between predictions and measurements is very good.

5 Global OMP properties

In Figs.6(a) and 6(b) are shown the real and imaginary components of our neutron and proton OMPs through their volume integrals J_V/A and J_W/A, respectively, as functions of incident energy.

In each plot for J_V/A, two curves are shown; the dashed line represents the smooth Hartree-Fock component, and the continuous curve is the sum of the HF and dispersive components. The DR components are calculated including the non-locality of the surface absorption.

In each plot for J_W/A, three curves are shown; the dotted line is for volume absorption, the dashed line is for surface absorption, and the continuous curve represents the sum of these two components. It is interesting to notice that the competition between surface and volume absorption at low incident energies

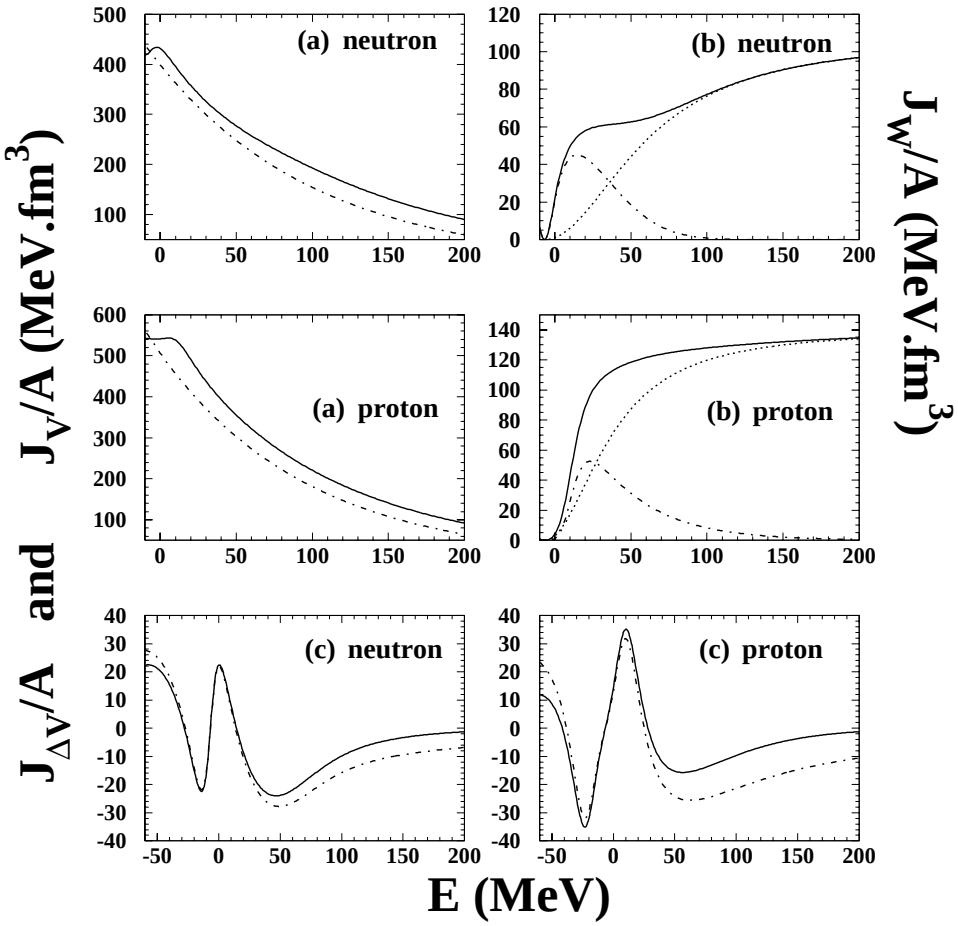

Figure 6: Volume integrals of the real potentials (a) and imaginary potentials (b). In (c) are shown the volume integrals for the surface dispersive terms with (continuous curves) and without (dashed curves) inclusion of non-locality.

depends upon the probe. These features probably reflect target structure effects.

In Fig.6(c) are shown the volume integrals $J_{\Delta V}/A$ of the DR surface terms for incident protons and neutrons. The continuous curves are obtained including non-locality in the CC calculations. The dashed curves are for CC calculations in which the range of non-locality is set to zero.

The effect of including the non-locality in the calculations is a weakening of the dispersive terms as E increases.

6 Conclusion

In this work we have presented a dispersive CC analysis of nucleon scattering and reaction measurements up to approximately 200 MeV for deformed nuclei with $A = 181$ - 186. The excellent overall agreement obtained between predictions and experimental data would not have been possible without including dispersive terms in the calculations. The range of non-locality, $1.2 \leq \beta \leq 1.4 fm$, has been deduced for the surface absorption. Obviously, new high precision scattering and reaction measurements for the W isotopes (and other deformed nuclei) up to 200 MeV are necessary to establish our analysis on firmer grounds and confirm our present results.

References

[1] C.Mahaux and R.Sartor, Adv. Nucl. Phys. **vol. 20**, 1 (1991)

[2] F.Perey and B.Buck, Nucl. Phys. **32**, 353 (1962)

[3] C.Mahaux, H.Ngô and G.R.Satchler, Nucl. Phys. **A449**, 354 (1986)

[4] J.Raynal, code `ECIS95`, unpublished.

[5] R.W.Finlay *et al.*, Phys. Rev. C **47**, 237 (1993)

[6] J.P.Delaroche *et al.*, Phys. Rev. C **23**, 136 (1981)

[7] B.G.Lay *et al.*, Phys. Rev. C **32**, 440 (1985)